Research Article | Vol. 30, No. 17 / 15 Aug 2022 / Optics Express 30592
Optics EXPRESS

Thin-film lithium niobate polarization modulator without polarization diversity

XUERUI SUN,[1,4] YINAN WU,[1,4] CHUANYI LU,[1] HAO LI,[1] XIAONA YE,[1] YUTING ZHANG,[1] SHIJIE LIU,[1] YUANLIN ZHENG,[1,2,5] AND XIANFENG CHEN[1,2,3,*]

[1] *State Key Laboratory of Advanced Optical Communication Systems and Networks, School of Physics and Astronomy, Shanghai Jiao Tong University, Shanghai 200240, China*
[2] *Shanghai Research Center for Quantum Sciences, Shanghai 201315, China*
[3] *Collaborative Innovation Center of Light Manipulation and Applications, Shandong Normal University, Jinan 250358, China*
[4] *These authors contributed equally to this work.*
[5] *ylzheng@sjtu.edu.cn*
[*] *xfchen@sjtu.edu.cn*

Abstract: With the development of photonic integrated circuits and optical information processing on thin-film lithium niobate (TFLN), the realization of the TFLN-based polarization device is becoming more and more crucial. Here, we demonstrate a polarization modulator on the TFLN platform without polarization diversity. Without polarization manipulation elements, the device only composes a phase modulator and a two-dimensional grating coupler. The structure features small footprint and high fabrication tolerance. The device holds promise for polarization encoding telecommunication.

1. Introduction

As one essential property of electromagnetic field, the state of polarization can be used to encode, calculate, and process information using light [1] and reflects a wealth of applications in optical perception and operation. Effectively manipulating light field at micro/nanoscales and realizing integrated optical devices are of great significance. Effective modulation of optical polarization states has exploited superb capabilities in a wide breadth of sciences and applications [2], such as optical communication [3–5], optical sensing [6–8], quantum entanglement [9–11] and so on. However, conventional polarization operation approaches often depend on large volume bulk optical elements, including waveplate-type and optical fiber circular polarization controller. It is a priority to implement polarization manipulation on the integration under the urgent demands of compactness, device stability and high-speed response.

Currently, thin-film lithium niobate (TFLN) has attracted considerable attention both in academics and industry. TFLN exhibits a huge potential in achieving high-density integration and ultrahigh-speed response, which benefits from strong light confinement caused by the high refractive index contrast of TFLN and the large electro-optical coefficient of lithium niobate (LN). These characteristics makes TFLN one of key candidates for the next-generation photonics integration platforms. TFLN-based EO modulators feature ultra-compactness, high-speed operation, low half-wave voltage, as well as low power consumption down to tens of fJ/bit or even lower [12,13]. In recent years, much efforts have been focused on TFLN-based electro-optic (EO) modulators. Various modulator paradigms with high performance have been realized in the dimensions of amplitude, phase, and frequency [12–21]. Despite the vast potential practicability, effective modulation of polarization is nevertheless still relatively limited for TFLN platform. Polarization manipulation elements on TFLN are considerably desired.

#468533 https://doi.org/10.1364/OE.468533
Journal © 2022 Received 21 Jun 2022; revised 21 Jul 2022; accepted 28 Jul 2022; published 4 Aug 2022

Optics EXPRESS

Originally, several typical on-chip integrated polarization processors comprising of polarization beam splitters (PBS) [22–25], polarization rotators (PR) [26–28], and polarization splitter-rotators (PSR) [29–33] have been extensively investigated on various platforms, which can realize the decomposition and conversion of linear polarization state in waveguides. These designs have been brought to the TFLN platform for polarization diversity, as devices on TFLN is intrinsically polarization dependent due to the material birefringence. Recently, a high performance polarization management device on TFLN has been reported [34], which utilizes PSR and Mach-Zehnder interferometer (MZI) as fundamental building blocks. Nevertheless, the modulation performance of this structure is highly dependent on the quality of the polarization diversity device, i.e., the PSR. The perfect implementation of PSR requires special design and precise accuracy, which aggravates the difficulty in fabrication. Additionally, the PSR with a 350-μm long length consequentially leads to a large device size.

In this Letter, we exhibit a TFLN-based polarization modulator utilizing a EO phase modulator and a two-dimensional grating coupler. The modulator avoids polarization diversity processor elements, which enormously improves the technological tolerance. We demonstrate effective modulation of polarization states with a polarization extinction ratio (ER) that is in excess of 16 dB for all the polarization output states and up to 35 dB for a subset of the operating points. In addition, mutually switching specified polarization states is also precisely realized.

2. Principle

The structure of the polarization modulator, as shown in Fig. 1(a), is composed of a one-dimensional grating coupler (1D GC), a multimode interferometer (MMI), an EO phase shifter and a two-dimensional grating coupler (2D GC). The waveguides and grating couplers are designed to support fundamental TE mode only. The configuration is fabricated on x-cut TFLN and the phase shifter is aligned along the y-direction to exploit the largest EO coefficient γ_{33} of LN (~27 pm/V@1550 nm). Considering the anisotropy of the x-cut TFLN, the output port is designed to separately balance the two arms in the y- and z-axis to minimize thermal shift. Three adiabatic tapers are inserted to connect the grating and the waveguide for fiber coupling. The input light is equally split into two arms by the MMI, whose phase is "pulled and pushed" by the EO phase shifter that utilizes a ground-signal-ground (G-S-G) traveling-wave electrode. Then the two arms are crossly combined and out-coupled by the 2D GC into fiber. The EO modulation results in a variable phase difference δ between the two arms, i.e., the two orthogonal polarization states at the 2D GC. As a consequence, the polarization state at the output port varies with the applied voltage, which moves along a great circular path through the poles on the surface of the Poincaré sphere. The schematic of the 2D GC is shown in Figs. 1(b) and 1(c). The

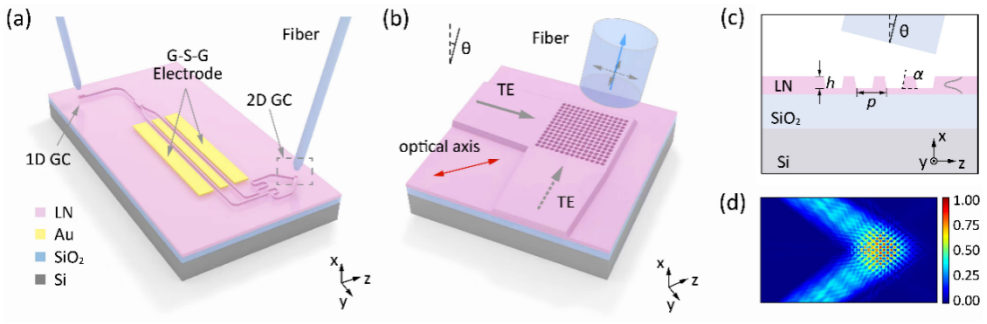

Fig. 1. (a) Schematic of the TFLN-based polarization modulator. (b) Schematic of the 2D GC, which is symmetric about the optical axis. θ: the diffraction angle. (c) Cross-sectional view of the 2D GC. (d) The simulation of wave propagation in the 2D GC at 1550 nm.

Optics EXPRESS

two orthogonal waveguides are symmetrical about the z-axis (i.e., the optical axis), and θ is the diffraction angle.

The high ER of the polarization modulation relies on the good performance of the MMI and 2D GC. Firstly, we investigate the tolerance of the MMI. The histogram in Fig. 2(a) shows the impact of the width and length variation of the MMI on its transmission. The MMI still maintains >96.8% in transmission when the width is swept from 2.6 to 3.0 μm and the length from 4.3 to 6.3 μm, which demonstrates superior fabrication tolerance for precision nanofabrication process. Figure 2(b) shows the simulated transmission spectrum when the width is 2.8 μm and the length is 5.3 μm. The simulated maximum transmission is 99.0%. The operation of the MMI covers a wide bandwidth over 100 nm at the telecommunication bands. The inset is the propagating mode in the MMI at the wavelength of 1550 nm.

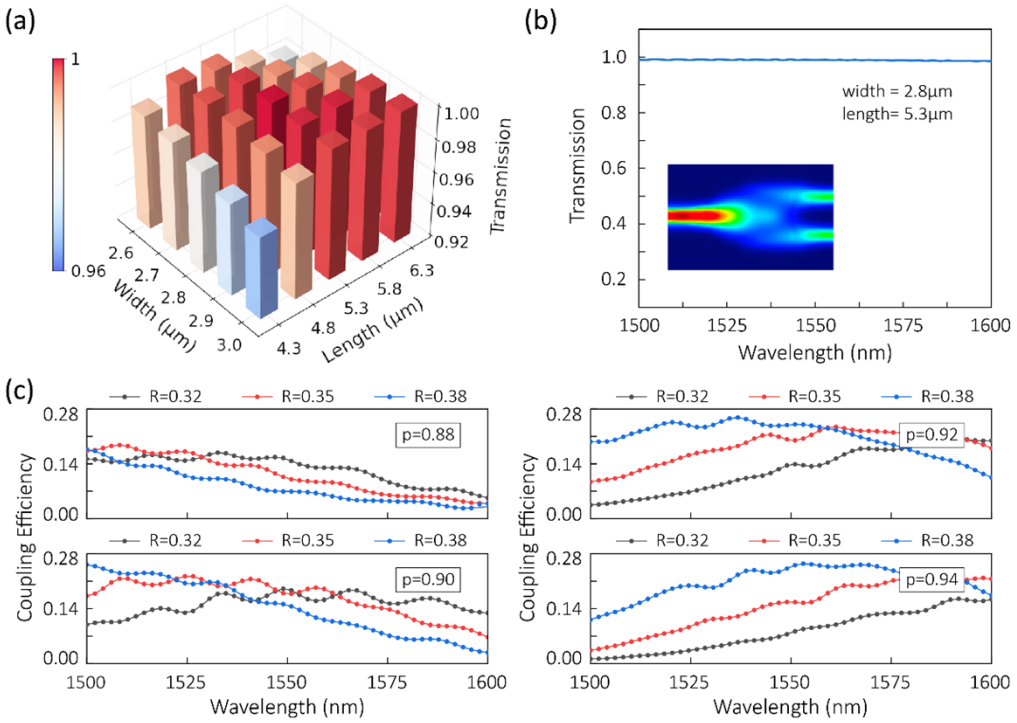

Fig. 2. (a) Transmission of the MMI with different widths and lengths. (b) Transmission spectrum of the MMI. (c) Calculated coupling efficiency as a function of wavelength.

Then, the parameters of the 2D GC are calculated and optimized by finite-difference time-domain (FDTD) simulation. The simulated normalized filed intensity at the 2D GC is shown in Fig. 1(d). There are three parameters that need to be optimized: the grating period p, the radius of the air hole R, and the etching depth h. To demonstrate the bandwidth of the 2D GC, the parameter sweep results on R and p are shown in Fig. 2(c). Taking into account the etching depth of the waveguides, h of 400 nm is adopted. Ultimately, the optimized set of parameters, $p = 0.92$ μm and $R = 0.38$ μm with air as the background, is found.

3. Device fabrication, characterization, and measurement

The designed polarization modulator is fabricated on commercial TFLN x-cut wafer (NANOLN) with a 600-nm thick top TFLN layer and 4.7-μm thick buried silica layer. To achieve the required

Optics EXPRESS

etching depth and sidewall roughness, a 580-nm-thick amorphous silicon (a-Si) is deposited by plasma enhanced chemical vapor deposition (PECVD) as a mask. Next, electron beam lithography (EBL) is used to define the 1D GC and the waveguide. The pattern is transferred to the a-Si mask and TFLN by inductively coupled plasma (ICP) etching. The residual a-Si is removed by aqueous dilution solution of KOH. Next, the 14 rows and columns of inverted cone air holes in the 2D GC is fabricated using the FIB milling method. It is worth mentioning that the one-step fabrication of 2D GCs along with LN waveguides has been demonstrated by optimized conditions during EBL and etching [35]. Then, the electrodes are patterned by ultraviolet (UV) photolithography and a 20-nm-thick Cr is evaporation-coated as an adhesion layer. Finally, a 200-nm thick Au layer is deposited on the surface via electronic beam evaporation and lift-off technique. The main part of the fabrication process was accomplished at the Center for Advanced Electronic Materials and Devices (AEMD), Shanghai Jiao Tong University.

Figure 3 displays the characterization of the fabricated polarization modulator device using scanning electron microscopy (SEM) and optical microscopy. The period of the 1D GC in Fig. 3(a) is 900 nm with a 33% duty cycle, aimed to maximum the coupling efficiency for the 1550 nm input. The footprint of the MMI is measured to be 2.8×5.3 μm^2, consistent with the theoretical analysis in Fig. 2. Both elements have the same cross section waveguide structure where the etching depth is about 350 nm with an inclination angle of about 65 degrees, as shown in Fig. 3(c). The top width of the waveguide is designed to 0.7 μm for single-mode propagation. Figure 3(d) shows the overall 2D GC structural SEM diagram, and the inset picture shows the details of the grating cells. Perforated in the coupling area, the appearance of the air hole forms inverted cone with about 400 nm depth whose parameters follow the calculation in Fig. 2(c). Finally, the optical microscopic image of the phase shifter section is shown in Fig. 3(e). The whole modulation length of the device covers 3 mm in this experiment, where the width of the signal electrode and the ground electrodes is 180 μm and 200 μm, respectively, and the electrode gap is 8 μm.

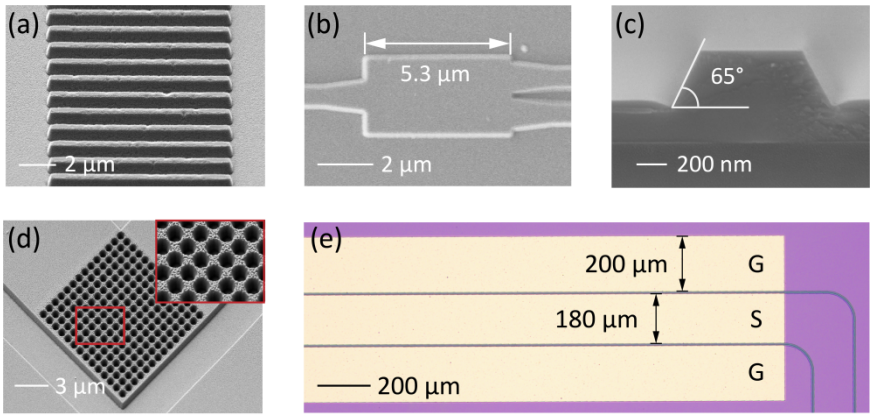

Fig. 3. Images of the details of the polarization modulator device: (a) grating coupler, (b) MMI, (c) cross section of the waveguide, (d) 2D GC, (e) push-pull electrode of the phase shifter.

The experimental setup is depicted in Fig. 4(a). An arbitrary waveform generator (AWG) acts as a signal source connected with a voltage amplifier to amplify the electrical signal. Then, the modulation signals are fed into the modulator at the input port by a probe. Meanwhile, light is emitted by an external cavity tunable continuous laser (New Focus, 1520–1570 nm) and amplified by an erbium-doped fiber amplifier (EDFA). The polarization of laser is controlled by polarization controllers (PC) to match the input 1D GC. The launch and collection of light

Optics EXPRESS

to the sample is achieved by vertical fiber coupling with a title angle of approximate 8 degrees. At the output part, a commercial polarization analyzer (PA) (Thorlabs PAX1000IR2/M) is used to characterize the generated polarization state. The fiber-to-fiber insertion loss of the device is measured to be approximately 17.5 dB at 1550 nm. The measured coupling loss of the 1D GC is 5.2 dB/facet, and that of the 2D GC is 11.5 dB/facet. Therefore, the on-chip loss of the polarization modulator is inferred to be 0.8 dB.

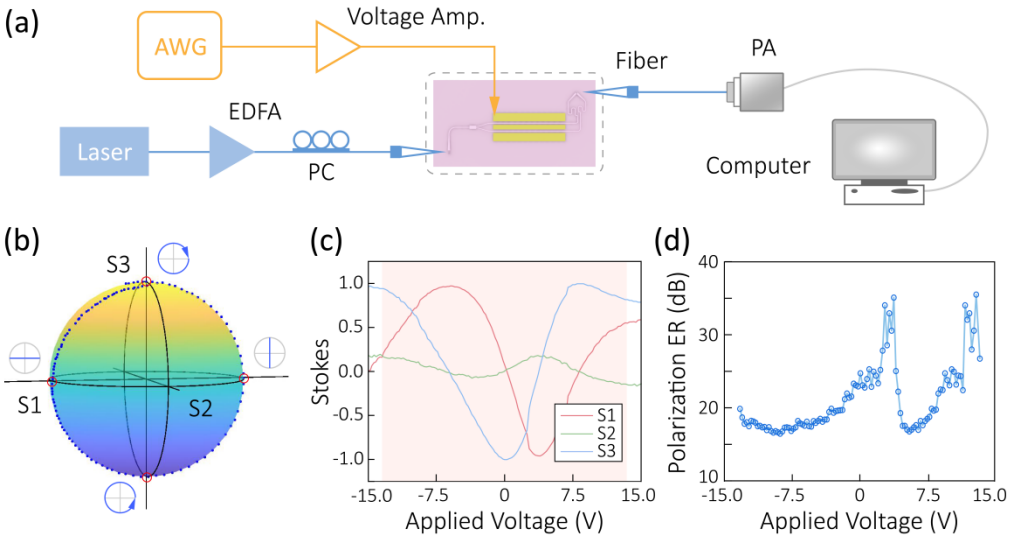

Fig. 4. (a) Experimental setup for the EO polarization modulation. The generated polarization states as plotted by (b) the Poincaré sphere and (c) the Stokes parameters. (d) Polarization extinction ratio as a function of the applied voltage.

The modulation performance of the device is shown in Figs. 4(b)–4(d). A sinusoidal wave is determined to modulate the optical signal, which is generated from AWG and amplified to a peak-to-peak value V_{PP} of 33 V. During the experiment, the output polarization state at zero voltage, which should be linearly polarized in theory, is measured to be left-handed polarized. This may be due to a tiny length difference between the two arms or polarization change in the out-coupling fiber. To quantitatively analyze the output polarization state, the Stokes vector measurements are adopted whose results are described by the Poincaré sphere, as shown in Fig. 4(b). After successive measuring the polarization state, the variations of three stoke parameters (S1, S2, and S3) are depicted in Fig. 4(c), where the Stokes vectors of each sampling point monitored by PA constitute a three-dimensional coordinate on the surface of Poincaré sphere. A set of polarization state round quasi-circle on the Poincaré sphere is extracted to intuitively demonstrate the modulation process, which is marked by blue points in Fig. 4(b) and related to the pink region in Fig. 4(c). The subset of these points is smaller than the output results produced by the modulation, i.e., the quality factor $V_\pi L$ for the device is less than 4.95 V·cm. Specially, the polarization path runs through the H, V, L and R states on the Poincare sphere, respectively, as marked by red circles in Fig. 4(b). Obviously, the precise modulation can flexibly generate arbitrary orthogonal basic polarization vector attributed to the design of our modulator device. One way to quantify the discrepancy between the theoretical expectation and the experimental results is to examine the orthogonality of output states from the modulator [36]. Consequently, the polarization ER of the modulator can be defined as ER=-10log$((1+\mathrm{P_1}\cdot\mathrm{P_2})/2)$, where $\mathrm{P_1}$ and $\mathrm{P_2}$ are two orthogonal polarization states that are opposite on the Poincaré sphere in Fig. 4(b). Theoretically, the dot product of two states in polarization ER will be -1 that demonstrates

Optics EXPRESS

superior performance of the device. As indicated in Fig. 4(d), the experimental polarization ER is in excess of 16 dB for all the output polarization states, and the maximum polarization ER achieves 35 dB. The fluctuating extinction ratio results from the slight deviation of the output state compared with the ideal great circle.

To further demonstrate the quality of the polarization output by the modulator, we next adjust specified DC voltage to drive the device for generating right-handed and linear polarization states, and the corresponding measurements of stokes parameters are summarized in Figs. 5(a) and 5(b), respectively. It can be indicated that our modulator can precisely manipulate the polarization state with low polarization crosstalk and high stability. Then, we encode a square wave electrical signals to switch between right-handed and linear polarization states. Continuous sampling for 1 min at a frequency of 900 samples/min of the two states are plotted on the Poincaré sphere, and the results are accurately concentrated around the (0,0,1) and (1,0,0) coordinate, as depicted in Fig. 5(c). The quantitative acquisition of the stokes vector in Fig. 5(d) shows that our modulator can switch on the specified cycle path of Poincaré sphere at high precision without polarization diversity processor elements.

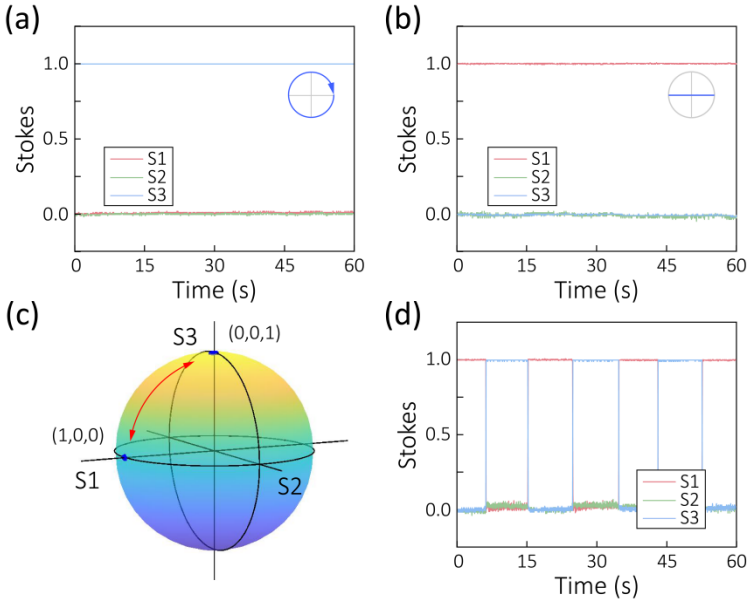

Fig. 5. The Stokes parameters of (a) the right-handed polarization state and (b) the linear polarization state. (c) The switching result that plotted on the Poincaré sphere. (d) The conversion of the Stokes parameters with the switch of the polarization states.

The performance of the device can be further improved by adjusting the electrical and optical elements. On the one hand, higher respond speed and lower drive voltage can be achieved by optimizing the electrode parameter to obtain a suitable characteristic impedance. For example, simulating the more suitable ratio between signal electrode width and the electrode gap is controllable, but fabricating a larger electrode thickness of the device is limited by our technical conditions at present. On the other hand, the width of the device can be further decreased. Moreover, the extra compensation for eliminating the unbalance between two arms at the output port can be substituted by applying a DC bias voltage to condense the scale of the modulator device.

Optics EXPRESS

4. Conclusions

In conclusion, a simple structure TFLN-based polarization modulator is designed and its relative complete functions are demonstrated. Instead of polarization diversity processor elements, an MMI structure is employed to split the input laser. To characterize the robustness of the modulator, high tolerance simulations are performed in terms of the scale of the device and the input wavelength. All the output polarization states obtain over 16 dB PER, and the maximum achieves 35 dB. Then, we demonstrate precise control of specific polarization state and effective switch between different polarization states. Notably, our work provides novel scheme of modulating polarization states on the TFLN platform, exhibiting huge potential for realizing ultra-compact and miniaturized optical systems at specified scenario, such as polarization encoded quantum key distribution.

Funding. National Natural Science Foundation of China (12074252, 12192252, 62005159, 62022058); National Key Research and Development Program of China (2017YFA0303701, 2018YFA0306301); Shanghai Municipal Science and Technology Major Project (2019SHZDZX01-ZX06); Shanghai Rising-Star Program (20QA1405400); Shanghai Jiao Tong University (21X010200828); Yangyang Development Fund.

Disclosures. The authors declare no conflicts of interest

Data availability. Data underlying the results presented in this paper are not publicly available at this time but may be obtained from the authors upon reasonable request.

References

1. Y. Intaravanne and X. Chen, "Recent advances in optical metasurfaces for polarization detection and engineered polarization profiles," Nanophotonics **9**(5), 1003–1014 (2020).
2. B. E. Saleh and M. C. Teich, *Fundamentals of Photonics* (Wiley, 2019).
3. D. Dai, C. Li, S. Wang, H. Wu, Y. Shi, Z. Wu, S. Gao, T. Dai, H. Yu, and H. K. Tsang, "10-Channel Mode (de) multiplexer with dual polarizations," Laser Photonics Rev. **12**(1), 1700109 (2018).
4. S. Chen, Z. Xie, H. Ye, X. Wang, Z. Guo, Y. He, Y. Li, X. Yuan, and D. Fan, "Cylindrical vector beam multiplexer/demultiplexer using off-axis polarization control," Light: Sci. Appl. **10**(1), 1–9 (2021).
5. Z.-Y. Chen, L.-S. Yan, Y. Pan, L. Jiang, A.-L. Yi, W. Pan, and B. Luo, "Use of polarization freedom beyond polarization-division multiplexing to support high-speed and spectral-efficient data transmission," Light: Sci. Appl. **6**(2), e16207 (2017).
6. R. Min, Z. Liu, L. Pereira, C. Yang, Q. Sui, and C. Marques, "Optical fiber sensing for marine environment and marine structural health monitoring: A review," Opt. Laser Technol. **140**, 107082 (2021).
7. P. Lu, N. Lalam, M. Badar, B. Liu, B. T. Chorpening, M. P. Buric, and P. R. Ohodnicki, "Distributed optical fiber sensing: Review and perspective," Appl. Phys. Rev. **6**(4), 041302 (2019).
8. M. Saha and S. Deb, "Analysis of highly efficient DFG in an electro-optic material exhibiting polarization rotation using TIR-based ORQPM technique," J. Nonlinear Opt. Phys. Mater. **31**(01), 2250001 (2022).
9. Y. Li, Y.-H. Li, H.-B. Xie, Z.-P. Li, X. Jiang, W.-Q. Cai, J.-G. Ren, J. Yin, S.-K. Liao, and C.-Z. Peng, "High-speed robust polarization modulation for quantum key distribution," Opt. Lett. **44**(21), 5262–5265 (2019).
10. K. Wei, W. Li, H. Tan, Y. Li, H. Min, W.-J. Zhang, H. Li, L. You, Z. Wang, and X. Jiang, "High-speed measurement-device-independent quantum key distribution with integrated silicon photonics," Phys. Rev. X **10**(3), 031030 (2020).
11. Z. Tang, Z. Liao, F. Xu, B. Qi, L. Qian, and H.-K. Lo, "Experimental demonstration of polarization encoding measurement-device-independent quantum key distribution," Phys. Rev. Lett. **112**(19), 190503 (2014).
12. C. Wang, M. Zhang, X. Chen, M. Bertrand, A. Shams-Ansari, S. Chandrasekhar, P. Winzer, and M. Loncar, "Integrated lithium niobate electro-optic modulators operating at CMOS-compatible voltages," Nature **562**(7725), 101–104 (2018).
13. M. Xu, M. He, H. Zhang, J. Jian, Y. Pan, X. Liu, L. Chen, X. Meng, H. Chen, and Z. Li, "High-performance coherent optical modulators based on thin-film lithium niobate platform," Nat. Commun. **11**(1), 1–7 (2020).
14. X. P. Li, K. X. Chen, and L. F. Wang, "Compact and electro-optic tunable interleaver in lithium niobate thin film," Opt. Lett. **43**(15), 3610–3613 (2018).
15. M. He, M. Xu, Y. Ren, J. Jian, Z. Ruan, Y. Xu, S. Gao, S. Sun, X. Wen, L. Zhou, L. Liu, C. Guo, H. Chen, S. Yu, L. Liu, and X. Cai, "High-performance hybrid silicon and lithium niobate Mach-Zehnder modulators for 100 Gbit s^{-1} and beyond," Nat. Photonics **13**(5), 359–364 (2019).
16. M. Mahmoud, L. Cai, C. Bottenfield, and G. Piazza, "Lithium niobate electro-optic racetrack modulator etched in Y-cut LNOI platform," IEEE Photonics J. **10**(1), 1–10 (2018).
17. Y. Liu, H. Li, J. Liu, S. Tan, Q. Lu, and W. Guo, "Low V_π thin-film lithium niobate modulator fabricated with photolithography," Opt. Express **29**(5), 6320–6329 (2021).

Optics EXPRESS

18. B. Pan, H. Cao, Y. Huang, Z. Wang, K. Chen, H. Li, Z. Yu, and D. Dai, "Compact electro-optic modulator on lithium niobate," Photonics Res. **10**(3), 697–702 (2022).
19. T. Ren, M. Zhang, C. Wang, L. Shao, C. Reimer, Y. Zhang, O. King, R. Esman, T. Cullen, and M. Loncar, "An integrated low-voltage broadband lithium niobate phase modulator," IEEE Photonics Technol. Lett. **31**(11), 889–892 (2019).
20. B. Pan, J. Hu, Y. Huang, L. Song, J. Wang, P. Chen, Z. Yu, L. Liu, and D. Dai, "Demonstration of high-speed thin-film lithium-niobate-on-insulator optical modulators at the 2-μm wavelength," Opt. Express **29**(12), 17710–17717 (2021).
21. X. Sun, Y. Wu, C. Lu, Y. Zhang, H. Li, S. Liu, Y. Zheng, and X. Chen, "Experimental investigation on the unbalanced Mach-Zehnder interferometer on lithium niobate thin film," Chin. Opt. Lett. **20**(10), 101301 (2022).
22. J. Huang, J. Yang, D. Chen, X. He, Y. Han, J. Zhang, and Z. Zhang, "Ultra-compact broadband polarization beam splitter with strong expansibility," Photonics Res. **6**(6), 574–578 (2018).
23. V. Zabelin, L. A. Dunbar, N. Le Thomas, R. Houdré, M. Kotlyar, L. O'Faolain, and T. Krauss, "Self-collimating photonic crystal polarization beam splitter," Opt. Lett. **32**(5), 530–532 (2007).
24. Z. Lin, K. Chen, Q. Huang, and S. He, "Ultra-broadband polarization beam splitter based on cascaded mach-zehnder interferometers assisted by effectively anisotropic structures," IEEE Photonics J. **13**(1), 1–9 (2021).
25. H. Xu, D. Dai, and Y. Shi, "Ultra-broadband and ultra-compact on-chip silicon polarization beam splitter by using hetero-anisotropic metamaterials," Laser Photonics Rev. **13**(4), 1800349 (2019).
26. H. Xu and Y. Shi, "Ultra-compact and highly efficient polarization rotator utilizing multi-mode waveguides," Opt. Lett. **42**(4), 771–774 (2017).
27. Z. S. Hou, X. Xiong, J. J. Cao, Q. D. Chen, Z. N. Tian, X. F. Ren, and H. B. Sun, "On-chip polarization rotators," Adv. Opt. Mater. **7**(10), 1900129 (2019).
28. F. Wang, Y. Chen, T. Ma, H. Liu, X. Wang, and C. Jin, "Mid-infrared polarization rotator based on a Si_3N_4-CaF_2 hybrid plasmonic waveguide with asymmetric metal claddings," Appl. Opt. **60**(8), 2441–2449 (2021).
29. Y. Ding, H. Ou, and C. Peucheret, "Wideband polarization splitter and rotator with large fabrication tolerance and simple fabrication process," Opt. Lett. **38**(8), 1227–1229 (2013).
30. W. D. Sacher, T. Barwicz, B. J. Taylor, and J. K. Poon, "Polarization rotator-splitters in standard active silicon photonics platforms," Opt. Express **22**(4), 3777–3786 (2014).
31. D. Dai and J. E. Bowers, "Novel concept for ultracompact polarization splitter-rotator based on silicon nanowires," Opt. Express **19**(11), 10940–10949 (2011).
32. H. Luo, Z. Chen, H. Li, L. Chen, Y. Han, Z. Lin, S. Yu, and X. Cai, "High-performance polarization splitter-rotator based on lithium niobate-on-insulator platform," IEEE Photonics Technol. Lett. **33**(24), 1423–1426 (2021).
33. Z. Chen, J. Yang, W.-H. Wong, E. Y.-B. Pun, and C. Wang, "Broadband adiabatic polarization rotator-splitter based on a lithium niobate on insulator platform," Photonics Res. **9**(12), 2319–2324 (2021).
34. Z. Lin, Y. Lin, H. Li, M. Xu, M. He, W. Ke, H. Tan, Y. Han, Z. Li, and D. Wang, "High-performance polarization management devices based on thin-film lithium niobate," Light: Sci. Appl. **11**(1), 1–9 (2022).
35. R. Ge, H. Li, Y. Han, L. Chen, J. Xu, M. Wu, Y. Li, Y. Luo, and X. Cai, "Polarization diversity two-dimensional grating coupler on x-cut lithium niobate on insulator," Chin. Opt. Lett. **19**(6), 060006 (2021).
36. J. D. Bull, N. A. Jaeger, H. Kato, M. Fairburn, A. Reid, and P. Ghanipour, "40-GHz electro-optic polarization modulator for fiber optic communications systems," in *Photonics North 2004: Optical Components and Devices* (International Society for Optics and Photonics 2004), pp. 133–143.